RSC Advances

ROYAL SOCIETY OF CHEMISTRY

PAPER

View Article Online
View Journal | View Issue

Cite this: *RSC Adv.*, 2026, **16**, 5743

Integrated proteomics, molecular dynamics, and *in vitro* characterization of antimicrobial peptide from *Lactobacillus acidophilus* vesicles against *Streptococcus mutans*

Venkatramanan Mahendrarajan and Nalini Easwaran*

Received 9th December 2025
Accepted 20th January 2026

DOI: 10.1039/d5ra09511e

rsc.li/rsc-advances

Membrane vesicles (MVs) released by probiotic bacteria such as *Lactobacillus acidophilus* have emerged as rich sources of bioactive peptides with antimicrobial properties. These MV-associated peptides represent a natural alternative to conventional synthetic antimicrobials, offering inherent selectivity and enhanced stability within complex microbial ecosystems such as the oral cavity. Given that *Streptococcus mutans* is a major etiological agent of dental caries due to its biofilm-forming and acidogenic capabilities, targeting it with probiotic-derived antimicrobial peptides (AMPs) presents a promising therapeutic avenue. In this study, the *L. acidophilus* MVs' peptide was tested against *S. mutans*, *in silico* and *in vitro*. Proteomic profiling of *L. acidophilus* MVs identified 143 unique peptides, of which several were predicted as AMPs by computational screening. A lead sequence, LTVTKAMNKVNKNAK, was prioritized for its non-hemolytic, non-toxic profile and favorable physicochemical traits. Molecular modelling and dynamics revealed membrane surface associated disruption against *S. mutans* by increased root mean square deviation (RMSD), root mean square fluctuation (RMSF) of the membrane, and water penetration count. The lead peptide exhibited an EC_{50} value of 1.1 mM and effectively inhibited biofilm formation while enhancing membrane permeability, thereby corroborating the *in silico* findings. These findings suggest that MVs from *L. acidophilus* can harbor AMPs capable of disrupting Gram-positive bacterial membranes through membrane disruption mechanisms.

1. Introduction

Dental caries is a major global public health problem affecting individuals across all age groups.[1] According to the Global Burden of Disease Study, untreated dental caries of permanent teeth is the most prevalent condition worldwide, with a high incidence particularly in low and middle income countries.[2] The etiopathogenesis of dental caries is primarily attributed to dysbiosis within the oral microbiome, where acidogenic and aciduric bacteria such as *Streptococcus mutans* play a central role.[3] *S. mutans* contributes to cariogenesis through several virulence mechanisms, including its ability to form robust biofilms, metabolize carbohydrates to organic acids, and synthesize extracellular polysaccharides that enhance adherence and biofilm stability.[4–6]

Traditional caries management relies heavily on mechanical debridement and chemical antimicrobial agents such as chlorhexidine and fluoride.[7,8] However, these treatments have limitations, including non-specific action, undesirable side effects, and increasing concerns about antimicrobial resistance and microbiome disruption.[9,10] In this context, antimicrobial peptides (AMPs) have emerged as promising therapeutic candidates.[11] AMPs are small, typically cationic and amphipathic molecules produced by a wide range of organisms as part of their innate immune defense.[12] They exhibit broad-spectrum antimicrobial activity, often by targeting microbial membranes, leading to pore formation, membrane thinning, or lipid disordering.[13] From a chemical perspective, AMP activity is governed by its physicochemical properties such as net positive charge, amphipathicity, hydrophobic moment, and secondary structure propensity, which collectively dictate affinity for anionic bacterial membranes.[14] Likewise, lipid chemistry, particularly the abundance of anionic phospholipids such as POPG and cardiolipin in the membrane creates electrostatic and hydrophobic interaction landscapes that facilitate selective peptide insertion and disordering.[15]

Recent studies have focused on identifying natural sources of AMPs from probiotic bacteria, including *Lactobacillus acidophilus*, which is widely recognized for its probiotic and health-promoting properties.[16] While some strains of *L. acidophilus* have been historically associated with late-stage caries progression, others demonstrate strain-specific antimicrobial effects against oral pathogens, particularly through secreted

---

School of Biosciences and Technology, Vellore Institute of Technology, Tiruvalam Road, Katpadi, Vellore-632014, Tamil Nadu, India. E-mail: nalini.e@vit.ac.in

metabolites and membrane vesicles (MVs).[17] MVs are nanoscale, bilayered extracellular structures released by both Gram-positive and Gram-negative bacteria and are increasingly recognized as vehicles for the delivery of bioactive molecules, including peptides, enzymes, and signaling factors.[18–20] Proteomic studies have revealed that MVs from probiotic bacteria such as *L. acidophilus* harbor peptides with antimicrobial, immunomodulatory, and antibiofilm activities.[21,22] Beyond their biological origin, MV associated peptides represent a chemically distinct class of AMPs. Unlike canonical AMPs that are often optimized for systemic host defense, MV associated peptides are naturally secreted, shorter, less hydrophobic, and frequently enriched in cationic and polar residues.[23] These chemical features make them more compatible with aqueous and biofilm-rich environments such as the oral cavity and may reduce cytotoxicity towards mammalian cells. This chemical novelty positions MV associated AMPs as an underexplored source for selective, biocompatible oral antimicrobials.[11] Computational screening of peptides derived from bacterial MVs has become a powerful approach to identify novel AMPs.[24] Advanced *in silico* tools such as the Database of Antimicrobial Activity and Structure of Peptides (DBAASP) and Collection of Antimicrobial Peptides (CAMP) allow high throughput screening based on machine learning algorithms and curated experimental data.[25,26] Moreover, toxicity and hemolysis prediction tools such as ToxinPred 3.0 and HemoPI 2.0 are essential for prioritizing peptides with therapeutic potential and minimal risk to host cells.[27,28]

Molecular dynamics (MD) simulations offer a powerful platform to investigate peptide membrane interactions at atomistic resolution.[29] Several studies have demonstrated that AMP activity is highly dependent on peptide orientation, conformation, and physicochemical properties, which determine the mode of membrane disruption ranging from carpet-like surface destabilization to transmembrane pore formation.[30] Despite the increasing catalog of bioactive peptides identified from probiotic and commensal bacteria, a critical knowledge gap remains in delineating how such MV associated peptides interact with bacterial membranes at an atomistic level.[31] Particularly for oral pathogens like *S. mutans*, the mechanistic understanding of AMP mediated disruption is scarce, limiting rational design and clinical translation of these molecules. Thus, integrating proteomic discovery with atomistic molecular dynamics and validating *in vitro* provides a powerful strategy to bridge this gap and accelerate AMP validation as next-generation oral therapeutics. In the present study, we performed proteomic screening of MVs derived from *L. acidophilus* MTCC 10307 and identified potential AMP candidates. The peptides were evaluated for antimicrobial potential using DBAASP and CAMP, and screened for hemolytic and toxic properties using HemoPI 2.0 and ToxinPred 3.0, respectively. We then constructed a biologically relevant model membrane representing *S. mutans*, incorporating 1-palmitoyl-2-oleoyl-*sn-glycero*-3-phospho-(1′-*rac*-glycerol) (POPG), cardiolipin (TOCL2), and phosphatidylethanolamine (POPE), based on established lipidomic data.[32,33]

Gram positive organisms such as *S. mutans* possess membranes enriched with cardiolipin and negatively charged phospho glycerol lipids, rendering lipid electrostatics a dominant chemical determinant of AMP binding and its associated disruption. This anionic lipid enrichment contrasts with the predominantly zwitterionic composition of mammalian membranes and provides a basis for selective AMP targeting. All-atom MD simulations were carried out to explore the interaction of the selected peptide with the modeled *S. mutans* membrane in perpendicular orientation.[34] Through comprehensive structural and dynamic analyses, Root Mean Square Deviation (RMSD), *z*-distance, Center Of Mass (COM) distance, contacts and hydrogen bond, we aimed to elucidate the mechanism by which the peptide perturbs the bacterial membrane. These insights provide mechanistic support for the use of MVs associated AMPs as targeted antimicrobial agents for oral health applications, with potential to combat biofilm-associated infections such as dental caries.

2. Materials and methods

2.1. Proteomics study of *L. acidophilus* MVs

The MVs isolated from *L. acidophilus* MVs MTCC 10307 were sonicated for 1 minute to release proteins, with approximately 50 µg of liberated protein treated in 100 µL of 7 M urea. To reduce disulfide bonds, 50 mM tris(2-carboxyethyl)phosphine (TCEP) was added and incubated at 37 °C for 1 hour. Then, 50 mM iodoacetamide (IAA) was introduced, mixed by vortexing, and incubated again at 37 °C for 30 minutes for alkylation. To lower the urea concentration in preparation for trypsin digestion, 25 mM NH_4HCO_3 was added. Trypsin was then added at a 1 : 30 enzyme-to-substrate ratio, and the samples were incubated at 37 °C for 16 hours. After digestion, samples were dried in a speed vacuum and reconstituted in 20 µL of Milli-Q water with 0.1% formic acid. For desalting, a Thermo Scientific C18 Pierce column was used. The resin was activated and equilibrated in 50% methanol/50% acetonitrile (ACN) and then in 5% ACN/0.5% TFA for 3–5 minutes. The reconstituted protein sample was applied to the resin and centrifuged for 3 minutes, followed by a wash with 0.5% TFA in 5% ACN. Elution was performed with 20 µL of 70% ACN, after which samples were dried in a speed vacuum and stored at −80 °C for LC-MS/MS analysis. For the LC-MS/MS, the mobile phases used were 0.1% formic acid in Milli-Q water (A) and 85 : 15 ACN in Milli-Q with 0.1% formic acid (B). Separation was achieved using a PepMap RSLC C18 analytical column (2 µm, 100 Å, 50 cm) and an Acclaim PepMap 100 pre-column (100 µm × 2 cm, nanoViper). The analysis was conducted on a Q Exactive Plus Biopharma mass spectrometer (Thermo Scientific).[35] The data were acquired using the software Thermo Scientific Xcalibur (version 4.2.28.14). The thermo raw files were converted into open mzML format using ThermoRawFileParser (1.4.5).[36,37] Then peptides were identified using MSGF+(2024.03.26) software by matching them with host protein sequences obtained from UniProt (*L. acidophilus*, Taxon ID: 1579).[38] Peptide identification was performed using MS-GF+ with default search parameters, assuming trypsin specificity and allowing up to two missed cleavages. Carbamidomethylation of cysteine was set as a fixed modification and methionine oxidation as a variable modification. A posterior error probability (PEP) cutoff of 0.01 was applied, corresponding to a 1% peptide level False Discovery Rate (FDR). Peptide confidence was further validated using a target-decoy strategy.[39] Then high confidence peptides were filtered using posterior error probability of 0.01 using OpenMS (3.3.0).[40] Then the AMPs were predicted in the Database of Antimicrobial Activity and Structure of Peptides (DBAASP) and CAMP server. The AMPs which got predicted in common by both servers are listed in a table and taken for further analysis.[25,26]

2.2. Peptide screening and toxicity evaluation

The hemolytic potential of these peptides was evaluated *in silico* using the HemoPI 2.0 server, which predicts hemolytic activity based on physicochemical and structural features.[28] The regression method was chosen which provides both a binary classification (hemolytic *vs.* non-hemolytic) and a regression-based HC_{50} value (μM) using Random Forest models trained on peptide sequence features.[41] Toxicity was assessed using the ToxinPred 3.0 webserver, which classifies peptides as toxic or non-toxic based on sequence-derived features.[27] Subsequently, the physicochemical properties including net charge, hydrophobicity, penetration depth and tilt angle were analyzed using the DBAASP platform. Further Boman index and GRAVY score was computed using APD6 online server.[42] Based on these evaluations, a lead peptide with favorable antimicrobial, non-toxic, and non-hemolytic properties was selected for further structural and functional analysis. Additional properties such as hydrophobic moment, isoelectric point, Boman index, and amphipathicity were also calculated to assess peptide folding propensity and functional selectivity toward bacterial over mammalian membranes.[25]

2.3. Protein and *Streptococcus mutans* membrane modeling

The three-dimensional (3D) structure of the selected lead peptide was predicted using the PEP-FOLD3 webserver, which employs *de novo* modeling based on structural alphabets. The generated structure was further validated using the Ramachandran plot analysis within BIOVIA Discovery Studio to assess stereochemical quality.[43]

For membrane modeling, a Gram-positive bacterial membrane representing *S. mutans* was constructed using the CHARMM-GUI membrane builder. A bilayer membrane was generated with 200 lipids in each leaflet to approximate native membrane dimensions. The lipid composition was selected based on literature-reported membrane profiles of *S. mutans*, comprising 65% POPG, 30% cardiolipin (TOCL2), and 5% POPE, in a 65 : 30 : 5 molar ratio.[44–46]

2.4. Molecular dynamics simulation of peptide–membrane system

MD simulations were performed using the GROMACS software package (v2024.1) with the CHARMM36m force field parameters, which were generated using the CHARMM-GUI interface.[47,48] The system was solvated with the TIP3P water model, and Na^+ and Cl^- ions were added to neutralize the system through the Monte Carlo ion replacement method. Energy minimization was performed using the steepest descent algorithm, followed by a 1 ns equilibration phase during which the system temperature was gradually increased from 100 K to 310.15 K. The temperature and pressure were maintained using the velocity-rescale thermostat and Berendsen barostat, respectively. Long-range electrostatics were calculated using the Particle Mesh Ewald (PME) method with a real-space cut-off of 1.2 nm, and van der Waals interactions were treated with a 1.2 nm cut-off. All covalent bonds involving hydrogen atoms were constrained using LINCS, allowing a 2 fs integration time step. Semi-isotropic pressure coupling was applied to maintain the membrane system under periodic boundary conditions.

An initial 500 ns MD simulation of the membrane alone (without peptide) was conducted in the *NPT* ensemble at 310.15 K and 1 atm to evaluate membrane stability. Subsequently, the peptide–membrane systems were simulated for 500 ns in perpendicular orientation to the membrane plane, to mimic possible physiological interactions and insertion behavior of the peptide. These simulations allowed for the detailed examination of peptide interactions and membrane disruption mechanisms.[49] A simulation length of 500 ns was selected as peptide membrane interactions typically require hundreds of nanoseconds to capture adsorption, reorientation, and insertion events as well as membrane perturbation. Prior atomistic studies of antimicrobial peptides report comparable timescales (200–500 ns) for stabilization and initial pore-forming behavior, while shorter simulations (<100 ns) generally do not reach mechanistic convergence. All MD simulations were run on a local workstation (Intel Core i7-14700K CPU, NVIDIA RTX 4070 GPU, 32 GB DDR5 RAM) using GROMACS 2024.2 with CUDA acceleration.

2.5. Simulation analysis parameters

Membrane specific parameters such as RMSD and root mean square fluctuation (RMSF) has been plotted for the membrane to assess the structural integrity.

For the peptide–membrane complexes, additional analyses were conducted including: RMSD, RMSF, peptide SASA, peptide *z*-distance (vertical insertion depth into the membrane), COM distance between peptide and membrane, number of contacts (<0.6 nm), and hydrogen bond between peptide and membrane throughout the simulation were analyzed. These analyses provided insights into the peptide's structural stability, orientation dynamics, and membrane-disruptive potential under simulated physiological conditions.[50]

2.6. Bacterium culture conditions, peptide synthesis and chemical characterization

S. mutans (MTCC 497) was sources from Microbial Type Culture Collection (MTCC), Chandigarh, India. They were regularly maintained and cultured on Luria Bertani (LB) media (HiMedia) at 37 °C for 24 hours.

The peptide LTVTKAMNKVNKNAK was synthesized *via* standard Fmoc-based solid-phase peptide synthesis (SPPS) on a rink amide resin using sequential coupling of protected amino acids (GenScript, USA). After chain assembly, the peptide was cleaved from the resin under acidic conditions and obtained as a TFA salt. The crude peptide was purified by reverse-phase high-performance liquid chromatography (RP-HPLC) to >99% purity (retention time: 7.60 min), and purity was verified at 220 nm. Peptide identity was confirmed by electrospray ionization mass spectrometry (ESI-MS) in positive ion mode, with an observed molecular weight of 1659.9 Da closely matching the theoretical mass of 1660.01 Da. The peptide was obtained as a white lyophilized powder and stored at −20 °C until use.

2.7. Hemolysis assay

Hemolytic activity was evaluated by incubating the peptide at a final concentration of 2.2, 1.1 and 0.55 mM in HiMedia, blood agar plates. The plates were incubated at 37 °C for 24 hours and any zone of hemolysis in the spot area was imaged and recorded.[51]

2.8. Cytotoxicity assay

The cytotoxic potential of the peptide was assessed *in vitro* using on 3T3 mouse fibroblast cells at three concentrations: 2.2, 1.1, and 0.55 mM. Cells were cultured in DMEM supplemented with 5% FBS until they reached approximately 80% confluence, then treated with the peptide in fresh DMEM for 24 hours at 37 °C and 5% CO_2. Following treatment, 100 µL of MTT solution (0.5 mg mL^{-1}) was added to each well and incubated for an additional 4 hours. The resulting formazan crystals were dissolved in 100 µL DMSO, and cell viability was determined by measuring the absorbance at 570 nm.[52] The percentage viability is calculated by the formula: % viability = treated OD/control OD × 100.

2.9. MIC and half-maximal effective concentration

The MIC and half-maximal effective concentrations (EC_{50}) for the synthesized peptide were determined as described earlier. 0.1OD culture of *S. mutans* were added with 6 to 0.047 mM concentration of peptide and incubated at 37 °C for 24 hours.[53] The MIC of tetracycline was also performed for positive control of the study. EC_{50} estimation was performed by fitting percent inhibition *versus* log-transformed concentration using a four-parameter logistic (4PL) model implemented in Python (SciPy). Model quality was assessed *via* residual analysis, determination of R^2 and RMSE, and bootstrap resampling ($n = 2000$) to obtain 95% confidence intervals. The top and bottom asymptotes were constrained to 100% and 0% inhibition, respectively. The EC_{50} obtained from the 4PL model was used to guide the selection of a representative concentration for downstream inhibition assays.[54]

2.10. Biofilm inhibition assay

The biofilm inhibition by peptide was screened using CV staining assay. Briefly 2.2, 1.1 and 0.55 mM of peptide was added with 0.1OD of *S. mutans* and incubated for 24 hours at 37 °C. The planktonic cells were removed carefully and the wells were washed with PBS. Then 0.1% crystal violet was used to stain the biofilm cells and unbound stain were removed by brief washing. The bound CV were eluted in 30% acetic acid and OD were recorded at 595 nm using a spectrophotometer.[55]

2.11. Membrane permeability assay

Membrane permeabilization was performed utilizing OD at 260 nm. 0.1OD cells of *S. mutans* were incubated with 2.2, 1.1 and 0.55 mM of peptide and incubated for 2 hours at 37 °C. The cultures were filtered using 0.22 µm syringe filters and the OD of filtrates were recorded at 260 nm. PBS was used as negative control and Triton X-100 was used as positive control for the experiment.[56]

$$\text{Membrane permeabilization } (\%) = \frac{\text{OD}_{260}\ \text{peptide}}{\text{OD}_{260}\ \text{Triton}} \times 100.$$

2.12. Bacterial permeability assay

Bacterial membrane permeability was evaluated using propidium iodide (PI) staining and flow cytometry. Mid-log phase *S. mutans* cells (equivalent to 1OD) were treated with the peptides at concentrations of 2.2 mM, 1.1 mM, and 0.55 mM for 2 hours at 37 °C. Following incubation, the cells were stained with 15 µg mL^{-1} PI for 15 minutes in the dark. The cells were then centrifuged to remove excess dye and resuspended in PBS. PI-positive events were gated from the FSC/SSC scatter plots and quantified as membrane-permeabilized cells. Flow cytometric analysis was performed using a CytoFLEX (Beckman Coulter, USA) system.[57]

2.13. Statistical analysis

In vitro experiments such as cytotoxicity, two-fold serial dilution, biofilm inhibition and membrane permeability assays were performed with three independent biological replicates. Data are presented as mean ± SD. Statistical analyses were performed in GraphPad Prism (version 8). One-way ANOVA was used to compare multiple groups, followed by a *post hoc t*-test for pairwise comparisons. Statistical significance was indicated using APA-style asterisks as follows: *$p < 0.05$, **$p < 0.01$, and ***$p < 0.001$. Parametric tests were used under the assumption of normally distributed data.

3. Results

3.1. Proteomic screening and AMP selection

Proteomic profiling of *L. acidophilus* MV fractions resulted in 143 unique peptides mapped against the host proteome. To evaluate their antimicrobial potential, peptides were screened through two curated AMP databases: DBAASP, which employs the Moon and Fleming hydrophobicity scale to assess membrane interaction potential, and CAMP, using the Random Forest algorithm both of which have been previously validated as reliable predictors of AMP functionality.

Table 1 Peptide identified from *L. acidophilus* MVs. Proteomics analysis of *L. acidophilus* MVs yields peptides that was predicted to have antimicrobial activity in two databases DBAASP and CAMP were presented with their physiochemical properties and hemolytic and toxicity predicted *in silico*

ID	Sequences	Length	Normalized hydrophobicity (Moon and Fleming)	Net charge	Penetration depth	Tilt angle	Grand average hydropathy value of the peptide	Boman index (kcal mol^{-1})	*In silico* hemolytic activity	*In silico* toxicity
1	LSSQIQNGAK	10	0.13	1	22	24	−0.63	1.74	Non hemolytic	Non toxin
2	RNAIVK	6	0.14	2	30	42	−0.23	2.72	Non hemolytic	Toxin
3	KAVREIIRYMKK	12	0.06	4	30	79	−0.717	2.95	Non hemolytic	Non toxin
4	SGVNHRFKK	9	1.02	3	30	39	−1.467	3.63	Non hemolytic	Toxin
5	YTFVWRKAVEKFHK	14	−0.1	3	17	56	−0.714	1.96	Non hemolytic	Non toxin
6	LTVTKAMNKVNKNAK	15	0.53	4	23	16	−0.653	1.88	Non hemolytic	Non toxin
7	RNIYSR	6	0.11	2	15	89	−1.68	5.85	Non hemolytic	Non toxin

Seven peptides predicted to have antimicrobial activity in both databases were shortlisted to improve prediction confidence and reduce false positives. To evaluate the safety profile of the identified AMPs, the peptides were subjected to *in silico* hemolytic activity screening using HemoPI 2.0, a machine learning-based predictive tool. The results indicated that all peptides were classified as non-hemolytic, with predicted HC_{50} values ranging from 134 to 221 μM, suggesting minimal risk of erythrocyte lysis at physiologically relevant concentrations. In parallel, potential peptide toxicity was assessed using ToxinPred 3.0, which employs advanced deep learning algorithms trained on experimentally validated toxic and non-toxic peptides. The analysis identified peptide 2 and peptide 4 as potentially toxic, whereas peptides including LTVTKAMNKVNKNAK, were predicted to be non-toxic. Among those peptides, the peptide LTVTKAMNKVNKNAK was prioritized based on its physicochemical characteristics: a net positive charge (+4), and a hydrophobicity profile conducive to membrane interaction, a chemical signature typical of membrane-active cationic peptides. Additionally, its penetration depth and tilt angle values, which are critical parameters in AMP membrane dynamics, suggested its ability to destabilize bacterial membranes.[3,4] Interestingly, the identified peptide (15 residues) falls within the ideal size range of cationic AMPs (10–30 residues) that balance penetrative ability with reduced aggregation risk, further supporting its classification as a functional AMP candidate (Table 1).

3.2. Peptide structure and membrane model construction

The 3D structure of LTVTKAMNKVNKNAK was modeled using PEP-FOLD3 and subjected to all-atom MD simulations (Fig. 1a). The predicted structure was validated by Ramachandran plot which depicted all the amino acids in the allowed region (Fig. 1b). The target membrane of *S. mutans* was constructed in CHARMM-GUI, with 200 lipids per leaflet (400 total), ensuring a biologically relevant bilayer size capable of accommodating full peptide insertion and realistic curvature. The membrane lipid composition POPG : TOCL2 : POPE in a 65 : 30 : 5 molar ratio was chosen based on literature reporting the dominance of anionic phospholipids (particularly POPG and cardiolipin derivatives like TOCL2) in *S. mutans* membranes.

3.2.1. Membrane dynamics in the absence of peptide. The membrane-alone simulation served as a baseline control for assessing intrinsic bilayer behavior. The RMSD increased from approximately 2.5 nm to ∼7 nm over 500 ns, plateauing between 6 and 7 nm only after ∼400 ns, indicating persistent large-scale fluctuations and late-stage structural stabilization (Fig. 2a). RMSF profiles revealed substantial lipid mobility with peaks ranging from 6–8 nm, reflecting dynamic headgroup and acyl chain motion (Fig. 2b).

The number of water molecules within the central bilayer region ($-1 < z < 1$ nm) remained stable throughout the trajectory, fluctuating narrowly between 5400 and 5600 molecules, indicating preservation of membrane integrity (Fig. 2c). Membrane thickness profiles showed two sharp and symmetric

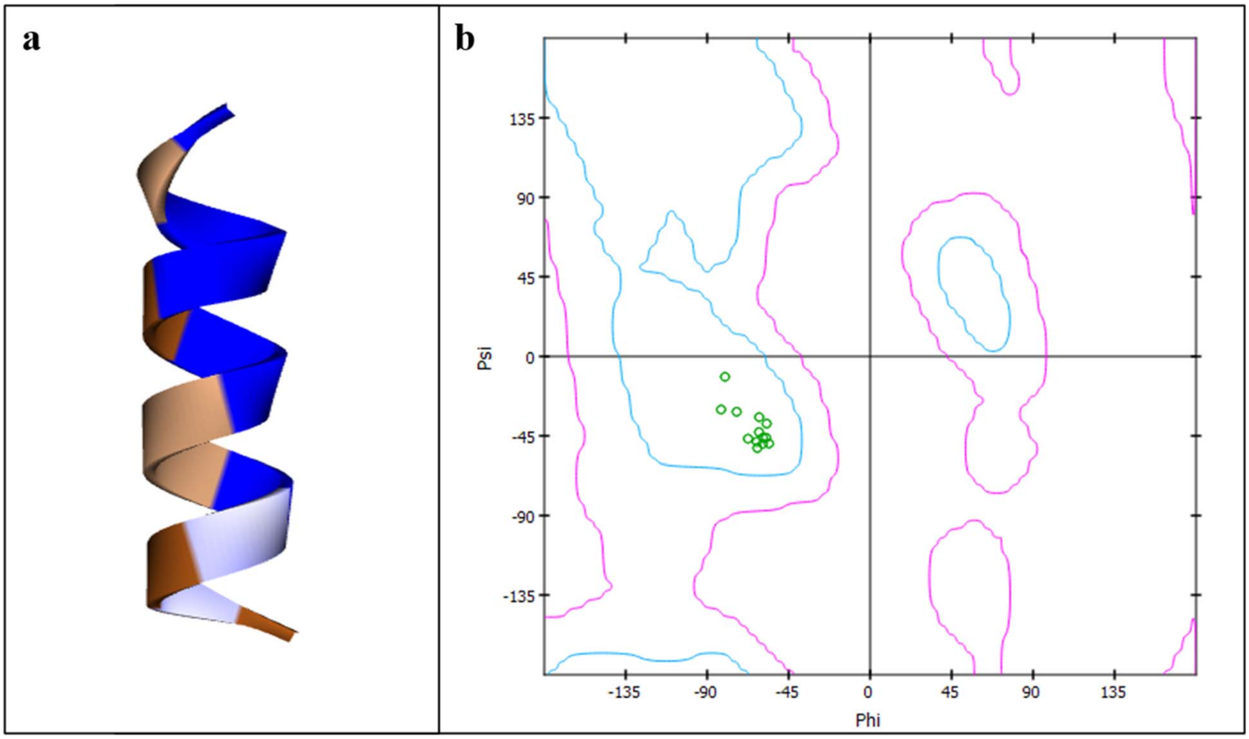

Fig. 1 Peptide structure prediction and validation. (a) The lead peptide structure was predicted and presented using BIOVIA Discovery Studio. (b) The Ramachandran plot of the lead peptide depicts all the amino acids were in the allowed region.

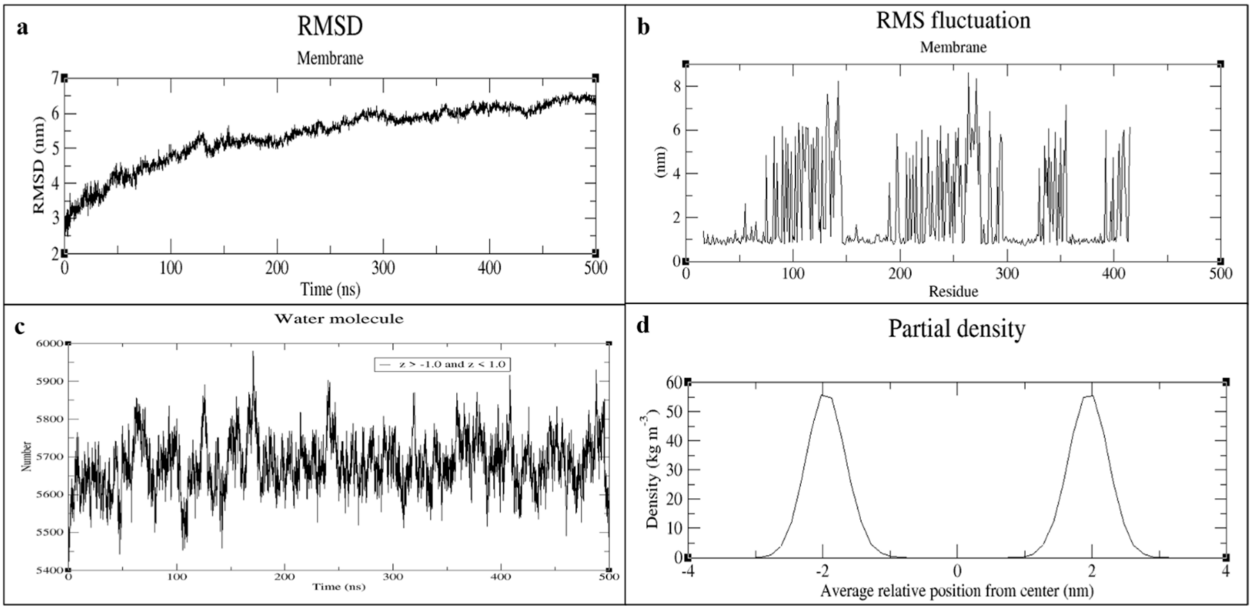

Fig. 2 Membrane alone dynamics. (a) RMSD of membrane alone over 500 ns, showing progressive increase and plateau. (b) RMSF of lipid residues, with high mobility in headgroup and acyl chains. (c) Number of water molecules in central bilayer ($-1 < z < 1$ nm), stable throughout simulation. (d) Phosphorus atom density across bilayer, showing symmetrical and well-defined membrane structure.

peaks, consistent with a well-defined Gram-positive bilayer (Fig. 2d).

3.2.2. Membrane dynamics in the presence of peptide. A 500 ns simulation of the peptide membrane was conducted to evaluate peptide-induced perturbations. The RMSD exhibited a steady increase beginning at approximately 3 nm and plateaued at 6–7 nm during the latter portion of the trajectory, indicating the membrane reached a dynamic equilibrium state

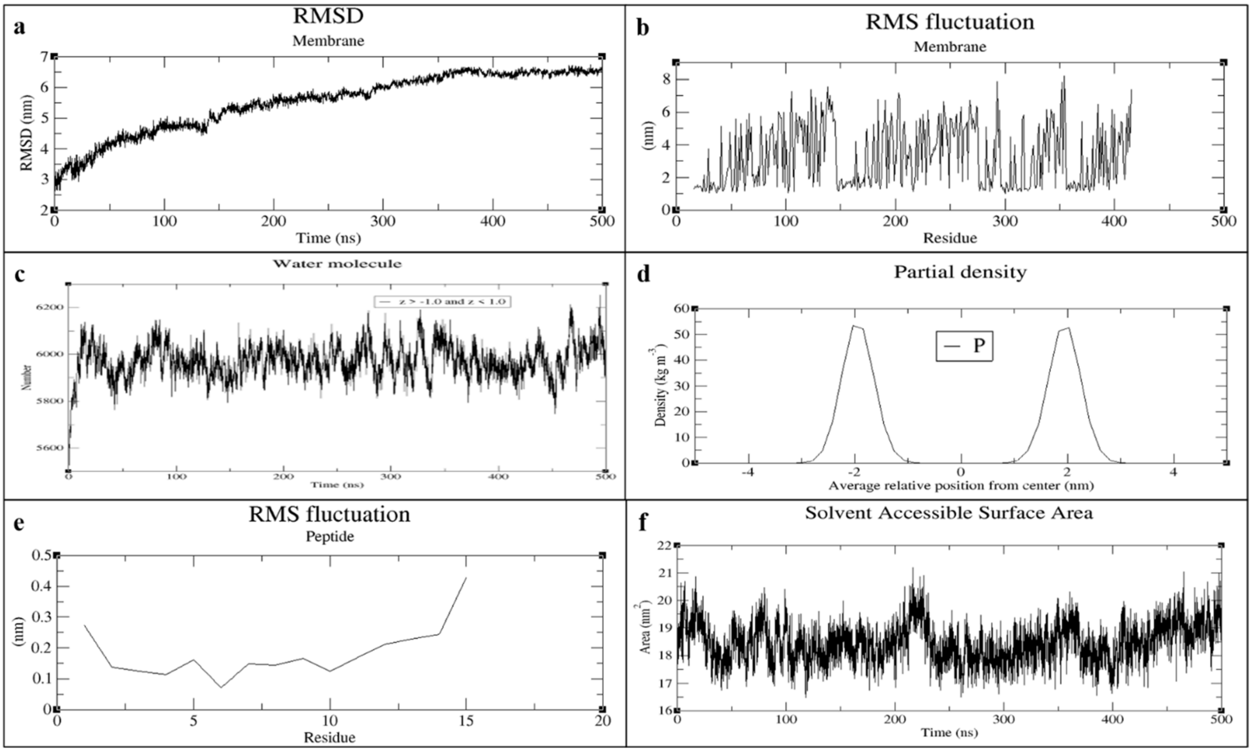

Fig. 3 Membrane peptide dynamics. (a) Membrane RMSD with peptide, plateauing after 400 ns. (b) RMSF of membrane with peptide, with enhanced fluctuations in lipid regions. (c) Water molecules in central region increase over time, indicating hydration/defect formation. (d) Phosphorus density profile shows partial bilayer deformation and loss of symmetry. (e) RMSF profile for peptide, indicating low residue fluctuation and stable peptide fold. (f) Solvent accessible surface area for membrane–peptide complex, showing increased exposure after 400 ns.

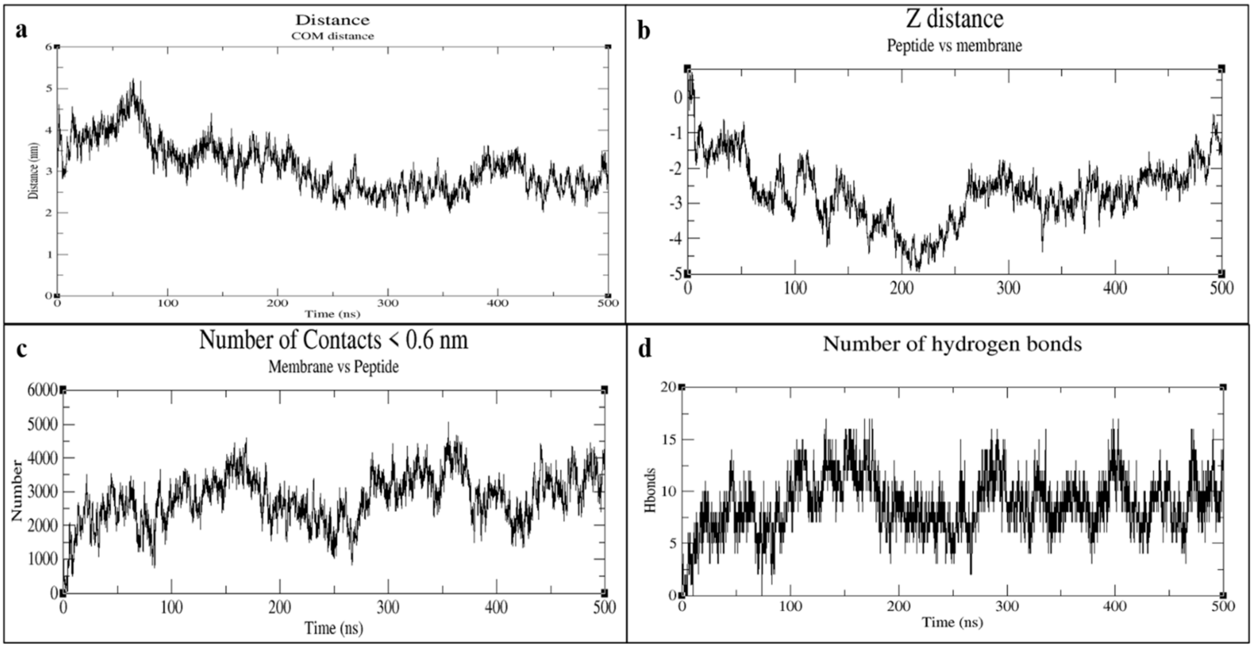

Fig. 4 Membrane peptide dynamics. (a) Time evolution of peptide–membrane center-of-mass distance, showing sustained association. (b) z-Axis position of peptide, indicating progressive insertion and stable embedding. (c) Number of atomic contacts (<0.6 nm) between peptide and membrane, increasing and remaining high. (d) Number of hydrogen bonds between peptide and membrane, with persistent formation and fluctuation.

characterized by sustained peptide-induced structural rearrangement (Fig. 3a). RMSF analysis showed notably elevated fluctuations, with several lipid regions displaying peaks exceeding 8 nm, significantly higher than the membrane-alone system. This enhanced mobility reflects localized destabilization and increased disorder in lipid packing caused by peptide interaction (Fig. 3b). The water molecule counts in the central membrane region started at ~5500 and gradually increased to ~6200 by the end of the simulation, contrasting sharply with the stable water profile in the membrane-only system. This increase suggests enhanced hydration, minor aqueous penetration, or transient defect formation triggered by peptide interaction (Fig. 3c). Membrane thickness plots demonstrated broader and less distinct phosphorus density peaks (Fig. 3d). In contrast, the peptide RMSF profile showed relatively low residue fluctuations (<0.4 nm), indicating maintained peptide structural integrity throughout the simulation (Fig. 3e). Solvent accessible surface area (SASA) for the total system exhibited dynamic variation between 17 and 21 nm^3, with occasional increases particularly after ~400 ns, revealing greater exposure of the membrane–peptide complex to solvent as the simulation progressed (Fig. 3f).

Interactions between the peptide and membrane were quantified by center of mass (COM) distance, *z*-axis displacement, number of hydrogen bonds, and contact frequency over a 500 ns simulation. The COM distance between the peptide and membrane fluctuated between 2.5 and 5 nm, with relative stability observed throughout the trajectory, indicating persistent peptide association with the bilayer surface (Fig. 4a). *z*-Axis distance analysis showed progressive peptide insertion, stabilizing at a displacement of approximately −4 nm for much of the simulation, suggesting the peptide penetrated and remained embedded in the membrane (Fig. 4b).

The number of atomic contacts (<0.6 nm) between the peptide and membrane lipids gradually increased and remained elevated (2000–5000 contacts), further supporting close association and substantial interaction surface between the peptide and bilayer lipids (Fig. 4c). Hydrogen bond analysis revealed formation and persistence of multiple peptide–membrane hydrogen bonds, averaging between 5 and 15 throughout the simulation, with transient peaks reaching up to 18. This indicates strong and dynamic interactions likely stabilizing the peptide in the bilayer (Fig. 4d).

Representative snapshots at 0, 250, and 500 ns, shown from both upright and side perspectives, highlight the temporal progression of the peptide's orientation and interaction with the membrane (Fig. 5a–f).

3.2.3. Chemical purity, identity, and structural properties. Analytical HPLC demonstrated that peptide exists as a chemically homogeneous species with a dominant peak accounting for >99.6% of the total peak area, consistent with high synthetic purity required for structural and biological studies (Fig. 6). MS analysis confirmed the expected protonated molecular ion and corresponding charge state distribution (*e.g.*, $[\text{M + H}]^+$, [M +

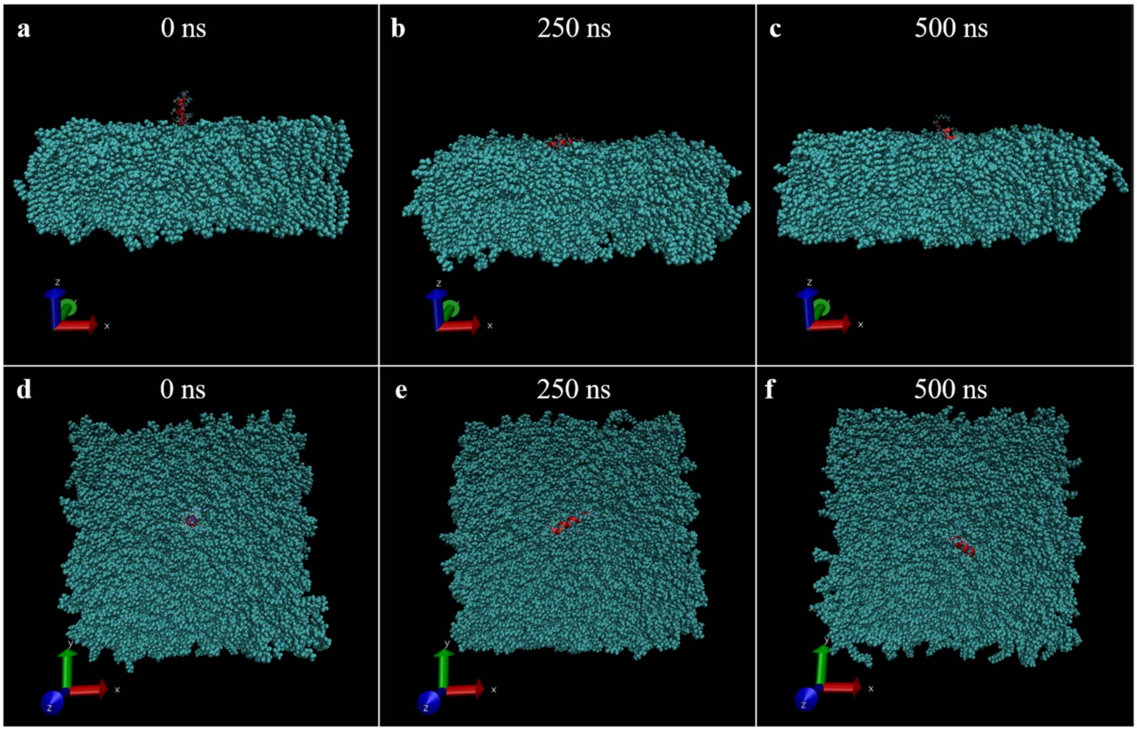

Fig. 5 Representative snapshots from the 500 ns MD simulation showing the interaction of the peptide with the *S. mutans* membrane. The peptide is shown in red and the membrane lipids in cyan. Panels (a–c) show side views at 0 ns, 250 ns, and 500 ns, illustrating peptide adsorption into the bilayer. Panels (d–f) show corresponding top-down (upright) views at the same time points. Coordinate axes indicate the simulation orientation (*x*–*y* plane = membrane surface; *z* = membrane normal). Together, the snapshots depict the temporal progression of peptide association with the membrane interface.

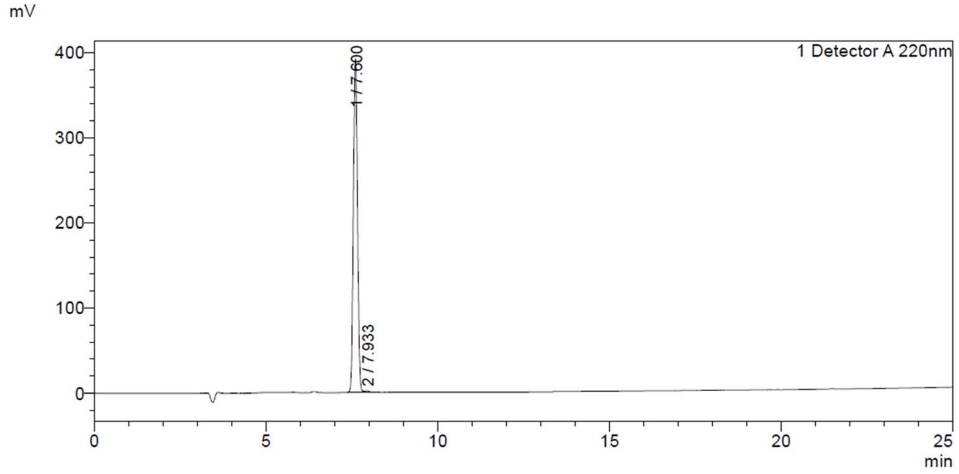

Fig. 6 Analytical RP-HPLC trace at 220 nm shows a single peak at ~7.6 min, confirming high chemical purity (>99%).

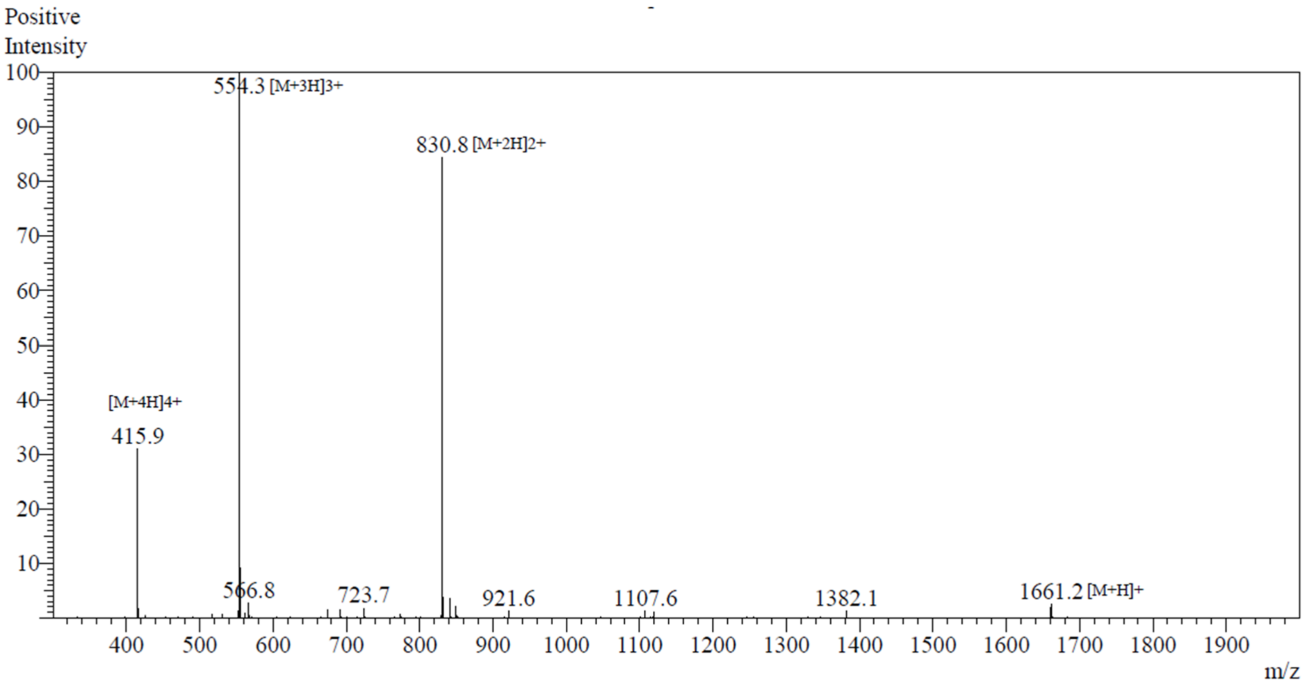

Fig. 7 ESI-MS spectrum (positive mode) confirms peptide identity through the monoisotopic protonated ion (*m*/*z* 1661.2 $[M + H]^+$) and expected charge state distribution ($[M + 2H]^{2+}$, $[M + 3H]^{3+}$, $[M + 4H]^{4+}$), consistent with the theoretical mass.

$2H]^{2+}$, $[M + 3H]^{3+}$, $[M + 4H]^{4+}$), verifying correct peptide assembly and deprotection (Fig. 7). Peptide is a 15-mer cationic rich in lysine and asparagine residues, giving it a net positive charge at physiological pH and contributing to its aqueous solubility and predicted membrane-interactive behavior. The absence of post-synthetic modifications (N-terminus free, C-terminus amidated *via* resin) supports its structural stability and compatibility with downstream assays.

3.3. *In vitro* toxicity screening

The peptides were evaluated for hemolytic and cytotoxic effects *in vitro*. At concentrations of 2.2, 1.1, and 0.55 mM, none of the peptides shown hemolysis on blood agar plates (Fig. 8a–c), whereas the positive control 1% Triton X 100 shows prominent hemolytic zone (Fig. 8d). Cytotoxicity assessment on 3T3 cells revealed high cell viability values of 97.29%, 96.33%, and 97.4% at 2.2 mM, 1.1 mM, and 0.55 mM concentrations, respectively (Fig. 9a).

3.4. *In vitro* antibacterial activity

The peptide exhibited an EC_{50} value of 1.1 mM against *S. mutans in vitro* (Fig. 9b). A four-parameter logistic (4PL) model was used to estimate the EC_{50} from the dose response inhibition data. The validated EC_{50} was 0.80 mM with a 95% bootstrap

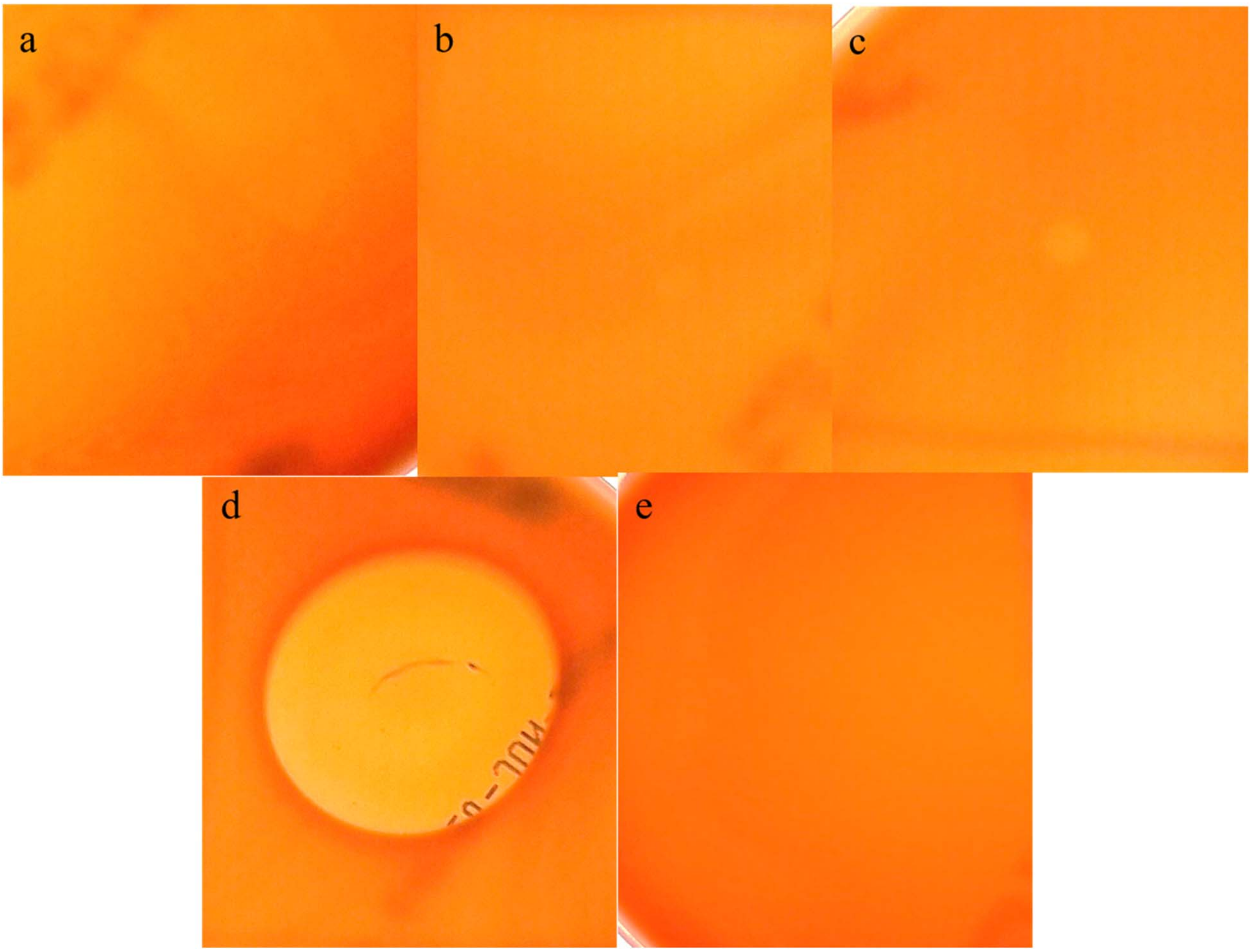

Fig. 8 Hemolytic activity of peptides at (a) 0.55 mM (b) 1.1 mM (c) 2.2 mM (d) positive control 1% Triton X 100 (e) negative control (PBS).

confidence interval of 0.52–1.13 mM and a Hill slope of 0.89. The model showed a good fit to the data ($R^2 = 0.93$; RMSE = 7.99). The 95% bootstrap confidence interval indicates that EC_{50} represents a concentration range rather than a single fixed value. Based on this range, an EC_{50} of 1.10 mM was selected as the representative midpoint and used for subsequent inhibition assays, as it fell within the validated interval and corresponded to the empirically observed midpoint of the inhibition curve (Fig. 9c). Residuals were evenly distributed around zero without systematic deviation, indicating that the 4PL model adequately described the data. The MIC against the positive control tetracycline was found to be 2 μg mL^{-1} for *S. mutans in vitro* (Fig. 9d). Biofilm formation was significantly inhibited in a dose-dependent manner, with inhibition rates of 64.91%, 53.03%, and 41.93% observed at 2.2 mM, 1.1 mM, and 0.55 mM peptide concentrations, respectively (Fig. 9e). Correspondingly, membrane permeabilization increased to 27.64%, 18.82%, and 13.56% at the same concentrations after 2 hours of treatment, indicating concentration-dependent disruption of the bacterial membrane integrity (Fig. 9f).

Membrane-compromised (dead) cells were quantified using PI staining by flow cytometry. Following 2 hours of peptide exposure at concentrations of 2.2, 1.1, and 0.55 mM, the proportions of dead cells were 25.87%, 16.86%, and 15.16%, respectively (Fig. 10a–d).

4. Discussion

In this study, we discovered a novel AMP, LTVTKAMNKVNKNAK, originating from *L. acidophilus* membrane vesicles, and validated its activity through computational and *in vitro* analyses. *In silico* safety assessment predicted the peptide to be non-hemolytic and non-toxic, supporting its potential therapeutic applicability. All-atom molecular dynamics (MD) simulations further demonstrated its ability to interact with and disrupt a model *S. mutans* membrane, suggesting a plausible mechanism of action consistent with known AMP membrane disruptive models. These findings are significant because they highlight the potential of probiotic MV derived peptides as biocompatible candidates for oral antimicrobial therapy, offering advantages over synthetic AMPs through natural biogenesis and compatibility with complex biofilm niches.

To ensure therapeutic safety, all peptides were assessed *in silico* for hemolysis and toxicity. HemoPI 2.0 predicted all peptides to be non-hemolytic, with HC_{50} values between 134 and 221 μM, indicating low potential to lyse human red blood

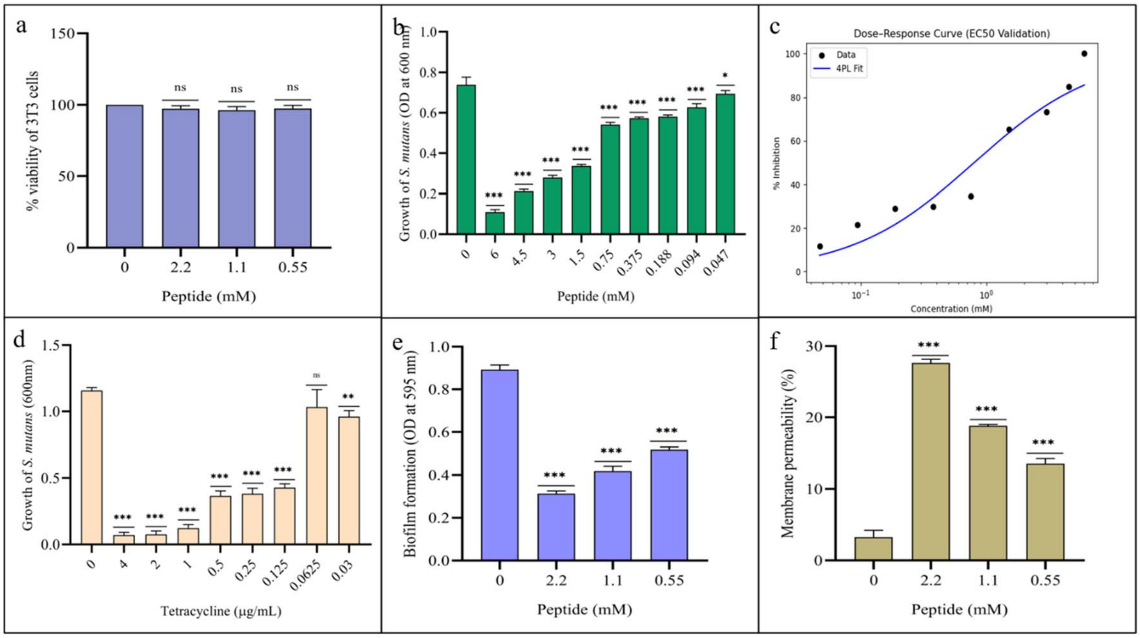

Fig. 9 (a) MTT assay show no associated cytotoxicity of peptides at 2.2, 1.1 and 0.5 mM concentration. (b) EC_{50} of the peptide was found to be 1.1 mM. (c) Dose response curve used for EC_{50} validation, percent inhibition was plotted against the log-transformed concentration and fitted with a four-parameter logistic (4PL) model (blue line). The EC_{50} determined from the fitted curve was 0.80 mM (95% bootstrap CI: 0.52–1.13 mM). The experimentally selected concentration of 1.10 mM lies within this window and corresponds to the midpoint of the inhibition profile. (d) MIC of tetracycline against the *S. mutans* was found to be 2 µg mL^{-1} which serves as the positive control. (e) The biofilm was inhibited up to 64.91%, 53.03%, and 41.93% at 2.2 mM, 1.1 mM, and 0.55 mM peptide concentrations. (f) Membrane permeability was increased to 27.64%, 18.82%, and 13.56% at 2.2, 1.1 and 0.55 mM peptide concentrations ($p < 0.001$ = ***, $p < 0.05$ = *, $p > 0.05$ = ns).

cells. ToxinPred 3.0 identified peptides 2 and 4 as potentially toxic, whereas peptides including the lead candidate LTVTKAMNKVNKNAK, were non-toxic. The cationic and amphipathic nature of the lead peptide likely contributes to its selectivity for bacterial membranes, which are anionic, over zwitterionic mammalian membranes.[58] These findings highlight its suitability for further antimicrobial evaluation. Unlike synthetic AMPs, MV-derived peptides benefit from natural biogenesis within probiotic vesicles, which may enhance their stability and functionality in complex biofilm niches.[21] Moreover, since *L. acidophilus* is a Generally Recognized as Safe (GRAS) organism, its MV associated peptides represent a promising source of biocompatible antimicrobials.[59] AMPs act primarily by disrupting microbial membranes, either by forming transient pores, inducing membrane thinning, or causing lipid disordering.[60–63]

In silico analysis revealed that the peptide engages the membrane primarily through surface association and partial insertion, inducing local lipid disorder without forming stable transmembrane pores. Increased lipid mobility and membrane hydration observed in the simulations suggest early-stage destabilization rather than catastrophic membrane rupture. This surface-driven perturbation is consistent with the mechanistic behavior of many cationic antimicrobial peptides that weaken membrane integrity through disordering, thinning, or interfacial disruption instead of pore formation. Importantly, this simulation-derived mode of action agrees with our experimental data, where the peptide caused concentration-dependent membrane permeabilization and PI uptake without overt cytotoxicity. Together, these results support a membrane-disruptive mechanism in which the peptide compromises *S. mutans* viability by perturbing lipid packing and weakening bilayer stability rather than forming defined pores.

The anionic nature of the membrane likely facilitated electrostatic attraction with the cationic peptide (+4 net charge), promoting initial surface interaction and eventual interactions. This is supported by the peptide's physicochemical properties such as moderate hydrophobicity, amphipathicity, and a suitable hydrophobic moment, all of which are known predictors of membrane activity.[64,65] The membrane model used in our study, composed of POPG, TOCL2, and POPE in a 65 : 30 : 5 molar ratio, is consistent with previously reported compositions for Gram-positive organisms, including *S. mutans*.[44–46]

The non-toxicity nature of peptide was confirmed *in vitro* through hemolysis and cytotoxicity assay. *In vitro* antimicrobial activity of the peptide LTVTKAMNKVNKNAK against *S. mutans* demonstrates its potential as a naturally occurring antibacterial agent, despite its relatively high effective concentration (EC_{50} = 1.1 mM). The observed dose-dependent inhibition of biofilm formation and increased membrane permeabilization suggest that the peptide exerts its effect primarily through membrane disruption, consistent with the membrane perturbation seen in molecular dynamics simulations.[66] The permeabilization was confirmed through PI staining in flow cytometry which enters the cell with disrupted cytoplasmic membrane.[67] Although the

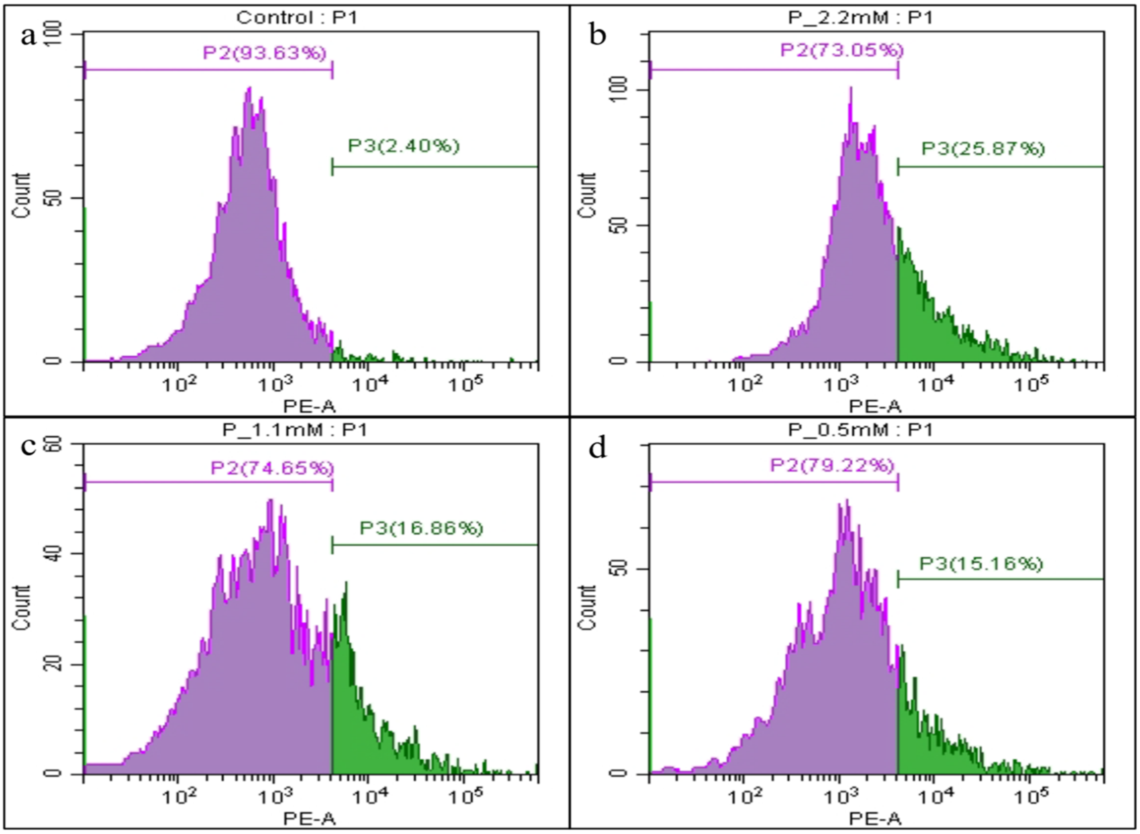

Fig. 10 Flow cytometry analysis revealed the membrane permeability at peptide concentrations of (a) 0 mM is 2.40% (b) 2.2 mM is 25.87% (c) 1.1 mM is 16.86 and (d) 0.55 mM is 15.16, which depicts the membrane permeabilization is proportional to the increasing concentrations of peptide.

inhibitory concentrations are higher compared to some synthetic or chemically modified AMPs, this peptide was isolated directly from *L. acidophilus* MVs without sequence optimization or chemical modification. Naturally occurring peptides often display moderate activity in their native form, the peptide reported in our study show higher concentration for MIC and EC_{50} which is a possible limitation of this study but possess desirable features such as biocompatibility and low cytotoxicity within biological environments. Moreover, the moderate potency may reflect a physiological role of MV-associated peptides in maintaining microbial balance rather than complete eradication of commensal species.[68,69] Importantly, the central value of this work lies not in immediate therapeutic potency but in demonstrating that probiotic MV-derived peptides can modulate Gram-positive membrane chemistry through a defined, surface-disruptive mechanism. Our peptide demonstrated moderate antimicrobial activity *in vitro* relative to more potent synthetic AMPs. Such higher potency benchmarks are primarily relevant to systemic antibiotics or optimized pharmaceutical peptides.[60] Similarly tetracycline used as a positive control in this study, exhibited a MIC of 2 μg mL^{-1} against *S. mutans in vitro*, but clinical use in the oral cavity requires localized formulations at far higher concentrations. So the topical tetracycline-HCl pastes and irrigations are typically applied at 100 mg mL^{-1} and maintain gingival crevicular fluid concentrations in the μg mL^{-1} range for ≥1 week *in vivo*, demonstrating that oral efficacy relies on high local payload, sustained exposure, and direct contact with dental biofilms rather than low MIC values alone.[70] Accordingly, the peptide's higher MIC/EC_{50} values remain within realistic bounds for localized dental delivery systems (*e.g.*, gels, varnishes, pastes, or slow-release coatings) where high concentrations are both feasible and clinically acceptable.[71] Importantly, the peptide is non-hemolytic, non-toxic, and membrane-selective, positioning it as a valuable scientific lead for understanding probiotic MV-derived antimicrobial mechanisms and for future peptide optimization rather than immediate clinical translation.[72]

Overall, the *in vitro* findings support the computational predictions and suggest that naturally secreted vesicular peptides from *L. acidophilus* can disrupt *S. mutans* membranes in a concentration-dependent manner. The observed membrane permeabilization aligns with the chemically predicted mechanism that cationic peptides disrupt Gram positive membranes *via* charge mediated adsorption followed by bilayer disordering rather than enzymatic inhibition.[60] These results lay the foundation for future peptide engineering or formulation approaches to enhance potency while preserving the natural selectivity of probiotic-derived AMPs. The activity of the peptide can be rationalized in terms of its chemical composition. The peptide contains multiple lysine residues contributing to a net +4 charge, enabling electrostatic attraction to the anionic POPG and cardiolipin headgroups in the *S. mutans* membrane. Moreover, the distribution of hydrophobic and polar residues imparts amphipathicity, a key chemical feature that promotes interfacial alignment and partial insertion into the bilayer. These chemical descriptors are consistent with the MD results, where peptide adopted a surface-oriented topology and induced lipid disordering, increased hydration, and leaflet thinning. The concordance between chemical properties, atomistic simulation, and biological membrane assays indicate a membrane chemistry driven antimicrobial mechanism. While the antimicrobial potency of LTVTKAMNKVNKNAK is moderate compared to synthetic AMPs, the significance of these findings is primarily conceptual. This work identifies probiotic membrane vesicles as natural reservoirs of short cationic peptides capable of modulating Gram-positive membrane electrostatics and bilayer order. Such mechanistic insight advances peptide biology and probiotic chemistry, independent of immediate clinical application. Moreover, future work should investigate whether LTVTKAMNKVNKNAK can synergize with other probiotic-derived antimicrobials or conventional treatments like fluoride, enhancing efficacy while reducing cytotoxicity or resistance pressure. Validation of activity in saliva-mimicking and biofilm conditions will also be essential to approximate the complex oral microenvironment. Future studies should explore sequence optimization, synergistic combinations with oral antimicrobials, and *in vivo* validation in multispecies oral biofilms to assess therapeutic potential.

5. Conclusion

The peptide LTVTKAMNKVNKNAK, identified from *L. acidophilus* MVs, demonstrated selective membrane-disruptive and antibacterial activity against *S. mutans* while remaining non-toxic. These findings support the concept of MV associated AMPs as precision antimicrobials for oral pathogen control. Moving forward, sequence optimization, formulation for topical oral delivery, and *in vivo* testing in biofilm-based caries models will be essential to enhance potency and translate these peptides toward practical therapeutic applications. Integration of proteomics, MD simulations, and experimental validation pipelines may further accelerate the discovery and development of MV associated AMPs as a new class of biocompatible oral therapeutics.

Author contributions

All authors contributed to the study conception and design. V. M. performed all the experiments and wrote the manuscript. N. E. finalized and edited the manuscript. N. E. supervised all the work performed.

Conflicts of interest

The authors have no relevant financial or non-financial interests to disclose.

Data availability

The data supporting this article have been included within this article.

Acknowledgements

The authors thank the Indian Council of Medical Research for the funding provided to this project (Project no. 5/4/2-6/Oral Health/2022-NCD-II). The authors also thank Vellore Institute of Technology for providing infrastructure to carry out the research. The funder played no role in study design, data collection, analysis and interpretation of data, or the writing of this manuscript.

References

1 V. Mahendrarajan, H. P. S. Lazarus, G. K. Muthukaliannan, S. Varghese and N. Easwaran, *Front. Oral Health*, 2025, **6**, 1607931, DOI: 10.3389/froh.2025.1607931.
2 Z. Li, C. Yu and H. Chen, *BMC Oral Health*, 2025, **25**, 715.
3 Y. Zhu, Y. Wang, S. Zhang, J. Li, X. Li, Y. Ying, J. Yuan, K. Chen, S. Deng and Q. Wang, *Front. Microbiol.*, 2023, **14**, 1162380.
4 J. A. Lemos, S. R. Palmer, L. Zeng, Z. T. Wen, J. K. Kajfasz, I. A. Freires, J. Abranches and L. J. Brady, *Microbiol. Spectrum*, 2019, **7**, DOI: 10.1128/microbiolspec.GPP3-0051-2018.
5 Z. Gao, X. Chen, C. Wang, J. Song, J. Xu, X. Liu, Y. Qian and H. Suo, *Microbiol. Res.*, 2024, **278**, 127526.
6 W. H. Bowen, R. A. Burne, H. Wu and H. Koo, *Trends Microbiol.*, 2018, **26**, 229–242.
7 J. Autio-Gold, *Operat. Dent.*, 2008, **33**, 710–716.
8 M. J. Y. Yon, S. S. Gao, K. J. Chen, D. Duangthip, E. C. M. Lo and C. H. Chu, *Dent. J.*, 2019, **7**, 37, DOI: 10.3390/dj7020037.
9 Z. L. S. Brookes, R. Bescos, L. A. Belfield, K. Ali and A. Roberts, *J. Dent.*, 2020, **103**, 103497.
10 G. P. Moran, L. Zgaga, B. Daly, M. Harding and T. Montgomery, *Toxicol. Lett.*, 2023, **379**, 11–19.
11 Q.-Y. Zhang, Z.-B. Yan, Y.-M. Meng, X.-Y. Hong, G. Shao, J.-J. Ma, X.-R. Cheng, J. Liu, J. Kang and C.-Y. Fu, *Mil. Med. Res.*, 2021, **8**, 48.
12 C. Bucataru and C. Ciobanasu, *Microbiol. Res.*, 2024, **286**, 127822.
13 F. Asif, S. U. Zaman, M. K. H. Arnab, M. Hasan and M. M. Islam, *Microbe*, 2024, **2**, 100051.
14 Z. Jiang, A. I. Vasil, J. D. Hale, R. E. W. Hancock, M. L. Vasil and R. S. Hodges, *Biopolymers*, 2008, **90**, 369–383.
15 A. L. Martin, P. N. Jemmett, T. Howitt, M. H. Wood, L. R. Cox, T. R. Dafforn, M. Campana, R. J. L. Welbourn, M. W. A. Skoda, L. A. Clifton, H. Hussain, J. L. Rawle, F. Carlà, C. L. Nicklin, T. Arnold and S. L. Horswell, *Soft Matter*, 2025, **21**, 7054–7073.
16 Y. Liu, H. Nawazish, M. S. Farid, K. Abdul Qadoos, U. E. Habiba, M. Muzamil, M. Tanveer, M. Sienkiewicz, A. Lichota and Ł. Łopusiewicz, *Fermentation*, 2024, **10**, 380, DOI: 10.3390/fermentation10080380.

17 D.-Y. Park, J. Hwang, Y. Kim, D. Lee, Y.-Y. Kim, H.-S. Kim and I. Hwang, *Sci. Rep.*, 2023, **13**, 7969.
18 M. Rima, M. Dakramanji, E. El Hayek, T. El Khoury, Z. Fajloun and M. Rima, *Heliyon*, 2025, **11**, e42509.
19 P. Aytar Çelik, K. Erdogan-Gover, D. Barut, B. M. Enuh, G. Amasya, C. T. Sengel-Türk, B. Derkus and A. Çabuk, *Pharmaceutics*, 2023, **15**, 1052, DOI: 10.3390/pharmaceutics15041052.
20 Q. Li, X. Chen, J. Xie and S. Nie, *Engineering*, 2025, **54**, 291, DOI: 10.1016/j.eng.2025.06.042.
21 S. N. Dean, M. A. Rimmer, K. B. Turner, D. A. Phillips, J. C. Caruana, W. J. Hervey IV, D. H. Leary and S. A. Walper, *Front. Microbiol.*, 2020, **11**, 710.
22 V. Mahendrarajan and E. Nalini, *J. Biomol. Struct. Dyn.*, 2025, 1–11.
23 C. Ciobanasu, *Antibiotics*, 2025, **14**, 414, DOI: 10.3390/antibiotics14040414.
24 Y. Fang, D. Fan, B. Feng, Y. Zhu, R. Xie, X. Tan, Q. Liu, J. Dong and W. Zeng, *Bioact. Mater.*, 2025, **50**, 510–524.
25 M. Pirtskhalava, A. A. Amstrong, M. Grigolava, M. Chubinidze, E. Alimbarashvili, B. Vishnepolsky, A. Gabrielian, A. Rosenthal, D. E. Hurt and M. Tartakovsky, *Nucleic Acids Res.*, 2020, **49**, D288–D297.
26 S. Thomas, S. Karnik, R. S. Barai, V. K. Jayaraman and S. Idicula-Thomas, *Nucleic Acids Res.*, 2010, **38**, D774–D780.
27 S. Gupta, P. Kapoor, K. Chaudhary, A. Gautam, R. Kumar and G. P. S. Raghava, *PLoS One*, 2013, **8**, e73957.
28 I. Abdelbaky, M. Elhakeem, H. Tayara, E. Badr and M. Abdul Salam, *BMC Bioinf.*, 2024, **25**, 368.
29 C. H. Chen, M. C. R. Melo, N. Berglund, A. Khan, C. de la Fuente-Nunez, J. P. Ulmschneider and M. B. Ulmschneider, *Curr. Opin. Struct. Biol.*, 2020, **61**, 160–166.
30 M. Pirtskhalava, B. Vishnepolsky, M. Grigolava and G. Managadze, *Pharmaceuticals*, 2021, **14**, 471, DOI: 10.3390/ph14050471.
31 A. Chaudhary, S. Bhalla, S. Patiyal, G. P. S. Raghava and G. Sahni, *Heliyon*, 2021, **7**, e06668.
32 M. E. MacGilvray, J. D. Lapek, A. E. Friedman and R. G. Quivey, *Microbiology*, 2012, **158**, 2133–2143.
33 K. Murzyn, T. Róg and M. Pasenkiewicz-Gierula, *Biophys. J.*, 2005, **88**, 1091–1103.
34 H. Itaya, K. Kasahara, Q. Xie, Y. Yano, K. Matsuzaki and T. Takahashi, *ACS Omega*, 2021, **6**, 11458–11465.
35 R. Prados-Rosales, L. Brown, A. Casadevall, S. Montalvo-Quirós and J. L. Luque-Garcia, *MethodsX*, 2014, **1**, 124–129.
36 N. Hulstaert, J. Shofstahl, T. Sachsenberg, M. Walzer, H. Barsnes, L. Martens and Y. Perez-Riverol, *J. Proteome Res.*, 2020, **19**, 537–542.
37 L. Martens, M. Chambers, M. Sturm, D. Kessner, F. Levander, J. Shofstahl, W. H. Tang, A. Römpp, S. Neumann, A. D. Pizarro, L. Montecchi-Palazzi, N. Tasman, M. Coleman, F. Reisinger, P. Souda, H. Hermjakob, P.-A. Binz and E. W. Deutsch, *Mol. Cell. Proteomics*, 2011, **10**, R110.000133, DOI: 10.1074/mcp.R110.000133.
38 S. Kim and P. A. Pevzner, *Nat. Commun.*, 2014, **5**, 5277.
39 J. E. Elias and S. P. Gygi, *Nat. Methods*, 2007, **4**, 207–214.
40 H. L. Röst, T. Sachsenberg, S. Aiche, C. Bielow, H. Weisser, F. Aicheler, S. Andreotti, H.-C. Ehrlich, P. Gutenbrunner, E. Kenar, X. Liang, S. Nahnsen, L. Nilse, J. Pfeuffer, G. Rosenberger, M. Rurik, U. Schmitt, J. Veit, M. Walzer, D. Wojnar, W. E. Wolski, O. Schilling, J. S. Choudhary, L. Malmström, R. Aebersold, K. Reinert and O. Kohlbacher, *Nat. Methods*, 2016, **13**, 741–748.
41 A. S. Rathore, N. Kumar, S. Choudhury, N. K. Mehta and G. P. S. Raghava, *Commun. Biol.*, 2025, **8**, 176.
42 G. Wang, C. Schmidt, X. Li and Z. Wang, *Nucleic Acids Res.*, 2025, **54**, D363–D374.
43 A. Lamiable, P. Thévenet, J. Rey, M. Vavrusa, P. Derreumaux and P. Tufféry, *Nucleic Acids Res.*, 2016, **44**, W449–W454.
44 S. Feng, S. Park, Y. K. Choi and W. Im, *J. Chem. Theory Comput.*, 2023, **19**, 2161–2185.
45 J. E. Custer, B. D. Goddard, S. F. Matter and E. S. Kaneshiro, *Lipids*, 2014, **49**, 543–554.
46 M. A. Bojanich and R. O. Calderón, *Arch. Oral Biol.*, 2017, **81**, 74–80.
47 J. C. Phillips, D. J. Hardy, J. D. C. Maia, J. E. Stone, J. V Ribeiro, R. C. Bernardi, R. Buch, G. Fiorin, J. Hénin, W. Jiang, R. McGreevy, M. C. R. Melo, B. K. Radak, R. D. Skeel, A. Singharoy, Y. Wang, B. Roux, A. Aksimentiev, Z. Luthey-Schulten, L. V Kalé, K. Schulten, C. Chipot and E. Tajkhorshid, *J. Chem. Phys.*, 2020, **153**, 44130.
48 J. Huang, S. Rauscher, G. Nawrocki, T. Ran, M. Feig, B. L. de Groot, H. Grubmüller and A. D. MacKerell, *Nat. Methods*, 2017, **14**, 71–73.
49 D. Sengupta, H. Leontiadou, A. E. Mark and S.-J. Marrink, *Biochim. Biophys. Acta, Biomembr.*, 2008, **1778**, 2308–2317.
50 W. Humphrey, A. Dalke and K. Schulten, *J. Mol. Graphics*, 1996, **14**, 33–38.
51 S. H. Lim, S. Mix, V. Anikst, I. Budvytiene, M. Eiden, Y. Churi, N. Queralto, A. Berliner, R. A. Martino, P. A. Rhodes and N. Banaei, *Analyst*, 2016, **141**, 918–925.
52 V. Mahendrarajan, H. Lazarus and N. Easwaran, *Heliyon*, 2024, **10**, e31898.
53 L. Andresen, T. Tenson and V. Hauryliuk, *Sci. Rep.*, 2016, **6**, 36549.
54 P. Virtanen, R. Gommers, T. E. Oliphant, M. Haberland, T. Reddy, D. Cournapeau, E. Burovski, P. Peterson, W. Weckesser, J. Bright, S. J. van der Walt, M. Brett, J. Wilson, K. J. Millman, N. Mayorov, A. R. J. Nelson, E. Jones, R. Kern, E. Larson, C. J. Carey, İ. Polat, Y. Feng, E. W. Moore, J. VanderPlas, D. Laxalde, J. Perktold, R. Cimrman, I. Henriksen, E. A. Quintero, C. R. Harris, A. M. Archibald, A. H. Ribeiro, F. Pedregosa and P. van Mulbregt, *Nat. Methods*, 2020, **17**, 261–272.
55 V. Mahendrarajan, G. K. Muthukaliannan and N. Easwaran, *Nat. Prod. Res.*, 2025, 1–8.
56 M. Zhang, L. Wang, W. Tang, Y. Xing, P. Liu and X. Dang, *Pest Manage. Sci.*, 2023, **79**, 3681–3692.
57 V. Mahendrarajan and N. Easwaran, *Biofouling*, 2025, **41**, 92–102.

58 L. T. Nguyen, E. F. Haney and H. J. Vogel, *Trends Biotechnol.*, 2011, **29**, 464–472.

59 J. María Remes Troche, E. Coss Adame, M. Ángel Valdovinos Díaz, O. Gómez Escudero, M. Eugenia Icaza Chávez, J. Antonio Chávez-Barrera, F. Zárate Mondragón, J. Antonio Ruíz Velarde Velasco, G. Rafael Aceves Tavares, M. Antonio Lira Pedrín, E. Cerda Contreras, R. I. Carmona Sánchez, H. Guerra López and R. Solana Ortiz, *Ther. Adv. Gastroenterol.*, 2020, **13**, 1756284820971201.

60 K. A. Brogden, *Nat. Rev. Microbiol.*, 2005, **3**, 238–250.

61 W. C. Wimley, *ACS Chem. Biol.*, 2010, **5**, 905–917.

62 L. Chen, W. Liu, Y. Li, S. Luo, Q. Liu, Y. Zhong, Z. Jian and M. Bao, *Int. Immunopharmacol.*, 2013, **17**, 108–115.

63 J.-L. Velasco-Bolom, G. Corzo and R. Garduño-Juárez, *J. Biomol. Struct. Dyn.*, 2018, **36**, 2070–2084.

64 C. D. Fjell, J. A. Hiss, R. E. W. Hancock and G. Schneider, *Nat. Rev. Drug Discovery*, 2011, **11**, 37–51.

65 W. C. Wimley and K. Hristova, *J. Membr. Biol.*, 2011, **239**, 27–34.

66 F. Lin, W. Jin, L. Yang, C. Tian, J. Zhang, Z. Jiao, J. Peng and G. Guo, *BMC Microbiol.*, 2025, **25**, 707.

67 I. D. Gbala, R. W. Macharia, J. L. Bargul and G. Magoma, *Molecules*, 2022, **27**, 4325, DOI: 10.3390/molecules27144325.

68 P. Anjana and S. K. Tiwari, *Front. Cell. Infect. Microbiol.*, 2022, **12**, 851140.

69 A. Mazumdar, Y. Haddad, V. P. Sur, V. Milosavljevic, S. Bhowmick, H. Michalkova, R. Guran, R. Vesely and A. Moulick, *Front. Microbiol.*, 2020, **11**, 1963.

70 L. A. Christersson, O. M. Norderyd and C. S. Puchalsky, *J. Clin. Periodontol.*, 1993, **20**, 88–95.

71 J. M. ten Cate, *Odontology*, 2006, **94**, 1–9.

72 R. E. W. Hancock and H.-G. Sahl, *Nat. Biotechnol.*, 2006, **24**, 1551–1557.